# Breaking Solvation Dominance of EC via Electron Engineering Enables Battery Operation Below -100℃

**Yuqing Chen**

Hunan University

**Qiu He**

Wuhan University of Technology

**Yun Zhao**

Tsinghua University    https://orcid.org/0000-0001-6003-3136

**WANG ZHOU**

Hunan University

**Peitao Xiao**

National University of Defense Technology

**Peng Gao**

Hunan University

**Naser Tavajohi**

Umeå University

**Jian Tu**

LI-FUN Technology Corporation Limited

**Baohua Li**

Tsinghua Shenzhen International Graduate School

**Xiangming He**

Tsinghua University    https://orcid.org/0000-0001-7146-4097

**Lidan Xing**

South China Normal University

**Xiulin Fan**

Zhejiang University    https://orcid.org/0000-0001-7294-480X

**Jilei Liu**（✉ liujilei@hnu.edu.cn）

Hunan University

---

**Article**

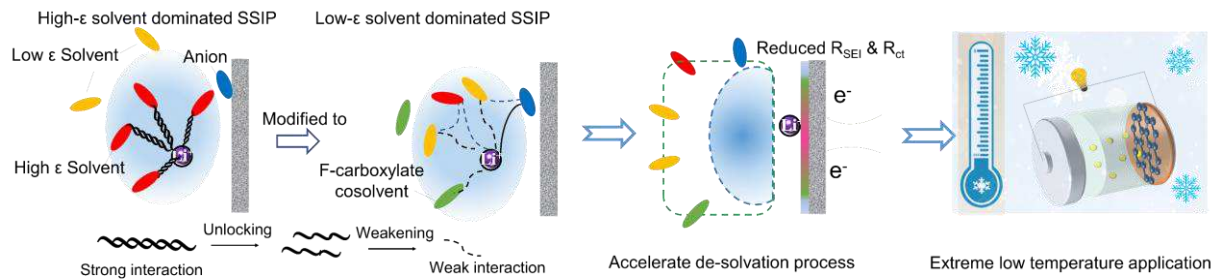**Additional Declarations:** There is **NO** Competing Interest.

---

# Breaking Solvation Dominance of EC via Electron Engineering Enables Battery Operation Below -100℃

Yuqing Chen[1], Qiu He[2], Yun Zhao[3], Wang Zhou[1], Peitao Xiao[4], Peng Gao[1], Naser Tavajohi[5], Jian Tu[6],

Baohua Li[3], Xiangming He[7], Lidan Xing[8], Xiulin Fan[9], Jilei Liu[1]*

TOC

## Abstract

The performance of current lithium-ion batteries (LIBs) is severely impaired by low temperatures, which require the development of powerful electrolytes with widen liquidity, facilitated ion diffusion ability, and lower desolvation energy. The keys lie in establishing mild interactions between $Li^+$ and solvent molecules internally, which is hard to realize in commercial ethylene carbonate (EC) based electrolytes due to the strong coordination of EC to $Li^+$. To address this challenge, we tailored the solvation structure with low-ε solvent dominated coordination and unlocked EC via electronegativity regulation of carbonyl oxygen. The modified electrolytes retain considerable ion conductivity (1.46 mS/cm) at -90 °C, remain liquid at -110°C, and facilitate $Li^+$ desolvation. Consequently, 4.5V graphite-based pouch cells perform stably with ~98% capacity retention and no lithium dendrite formation over 200 cycles at -10 °C. These cells also retain ~60% of their room-temperature discharge capacity at -70 °C, and miraculously remain functional even below -100 °C. This design strategy of breaking the solvation dominance of EC via electron engineering can be extended to other alkali-metal-ion batteries at extremely low temperature.

**Keywords**: Lithium-ion batteries, electrolyte, solvation structure, internal interaction, desolvation energy, low temperature.

## Introduction

High-voltage lithium-ion batteries (LIBs) capable of operating over a wide range of temperature are highly desirable for energy storage under extreme conditions such polar scientific expedition, high altitude station, and in certain military applications. However, several challenges lie in, including: i) limited liquid range of electrolyte[1], ii) slow mass transport, including poor conductivity and Li diffusivity in bulk materials[2, 3], especially graphite anodes; iii) sluggish charge transfer process resulting from high energy barriers for $Li^+$ desolvation and $Li^+$ migration within the SEI [2, 4, 5, 6, 7, 8, 9]. These

34  factors cause unwanted lithium plating or unfriendly SEI, causing low efficiency and

35  serious safety concerns[10, 11, 12, 13, 14, 15]. (**Fig. S1a**). Previous studies have shown that it

36  is charge transfer processes rather than mass transport that dominates the

37  electrochemical performance of LIBs under low temperature (LT) conditions (≤0 °C),

38  given the much higher energy barrier of the former[1, 8, 9, 16, 17]. This highlights the

39  importance of reducing the desolvation energy barriers in facilitating charge transfer[4,

40  6, 16]. Truly, the desolvation energy is highly dependent on the solvation structure of

41  electrolyte[9, 16, 18, 19]. And the keys of moderate desolvation process lie in promoting the

42  construction of a $Li^+$ solvation shell with weak interactions between $Li^+$ and solvents[9].

43      Strategies including liquefied gas electrolytes[20, 21], novel co-solvents[22, 23], highly

44  fluorinated solvents[4, 24], PC based electrolytes[25], local high concentration electrolytes

45  (LHCEs)[4, 8, 23, 26, 27], and weakly solvating electrolytes[4, 8, 9, 23, 25, 27, 28, 29], and co-

46  intercalation method[30] have been therefore proposed to optimize the solvation

47  structures. These strategies trend to promote more anion to solvate with $Li^+$ and mainly

48  rely on low dielectric constant (ε) solvents to replace EC, therefore facilitating

49  desolvation process. Among which, LHCEs appear to be particularly promising for LT

50  battery applications. These systems exploit the non-polarity of fluorinated ether diluent

51  to disrupt strong interactions between highly polar (high-ε) molecules in LIB electrolyte,

52  which broadens the liquid range of the electrolyte and promotes the desolvation process

53  (**Fig. S1b**). While these EC-free strategies succeed in lowering the desolvation energy,

54  they often neglect the direct interaction between relative high-ε solvents and $Li^+$, and

55  the good conductivity property owing to high-ε effect of EC could be sacrificed. This

56  limits the potential applicability of these strategies in further extreme low-temperature

57  environments.

58      In LIB electrolytes, $Li^+$ typically coordinates with polar solvent molecules in

59  carbonate electrolytes via an electronegative carbonyl oxygen. Theoretically, this

60  coordination could be weakened without sacrificing the high dielectric property (ε) of

61  polar solvents by reducing the carbonyl oxygen's electronegativity in high-ε solvents,

62  rather than replacing them with low-ε solvents. Speculatively, this could potentially be

63  achieved by introducing elements with strongly electron-withdrawing effect[16, 24], such

64  as fluorine, as an example strategy. Fluorination is expected to weaken the coordinative

65  interactions between high-ε solvents (e.g., cyclic carbonates) and Li$^+$ **(Fig 1a)**, resulting

66  in i) the release of more high-ε solvents, which would promote the coordination of low-

67  ε solvents (e.g., linear carbonates) with Li$^+$ to maintain occupancy of its coordination

68  sites, therefore the solvent separated ion pair (SSIP) would be converted from high-ε

69  solvent dominated to low-ε dominated one, and ii) unlocked interaction of the

70  remaining coordinated high-ε solvents **(Fig 1a).** Several merits can be therefore derived

71  from this unique solvation structure: i) overall coordinative interactions between Li$^+$

72  and solvents are significantly and thoroughly weakened, by impairing the coordination

73  number and strength of high-ε solvents and promoting a low-ε solvents dominated

74  solvation structure (**Fig. 1a**). In addition, the fluorinated carboxylate cosolvent also

75  participates in solvation via carbonyl group, even though its interaction with Li$^+$ is quite

76  weak (**Fig. 1a**). All these, together promote a desirable solvation structure with much

77  weaker interactions between Li$^+$ and all the electrolyte solvents. The structure of this

78  type is expected to be particularly advantageous for further widening liquid range and

79  further facilitated Li$^+$ desolvation. And ii) Fluorinated cosolvent benefits for F-rich SEI

80  formation due to the lower LUMO energy caused by fluorination[31] (**Table S2**).

81  Additionally, Fluorination can lower the electrolyte's HOMO energy, thereby widening

82  its electrochemical window and meeting demands for high voltage batteries [31, 32].

83  Altogether, this approach offers a more effective way to directly rejuvenate the desire

84  solvation structure that is expected to extend its application to further extremely low

85  temperatures.
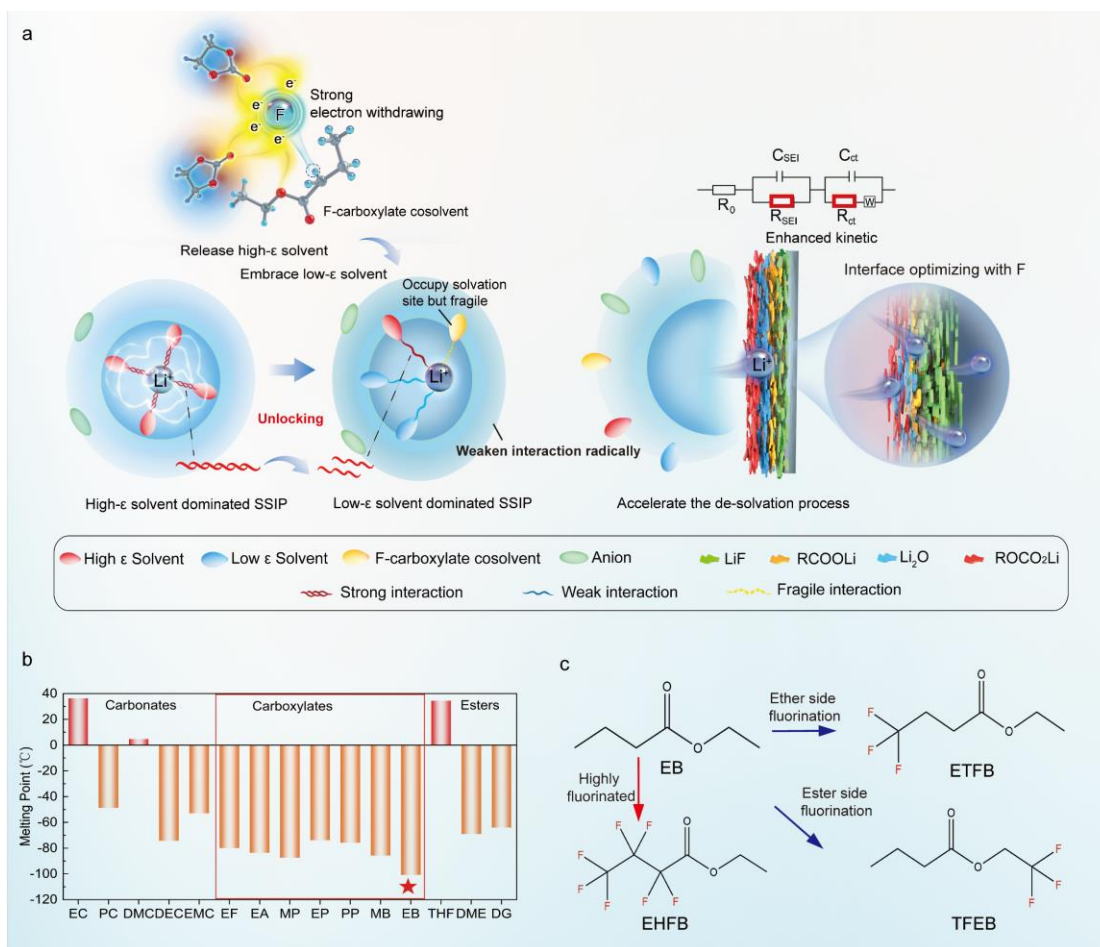
**Fig. 1: a, Proposed low temperature electrolyte design principle. b, Melting point of common carbonate and carboxylate solvents. c, Chemical structure of the selected EB and its fluorinated analog cosolvents.**

Bearing these in mind, we aimed to identify potential cosolvents for fluorination based on ethyl butyrate (EB), which has a rather low melting point (**Fig 1b, Fig S2**), as a promising candidate for LT electrolyte cosolvent. We proposed a series of high-performance LIB electrolyte recipes containing analogs of EB as cosolvents, including 4,4,4-ethyl trifluorobutyrate (ETFB), ethyl heptafluorobutyrate (EHFB) and 2,2,2-trifluoroethyl butyrate (TFEB), with varying fluorination degree and/or fluoride site (**Fig 1c, Fig. S3**). As expected, the co-solvent electrolyte recipes exhibit high ionic conductivity (1.4-14.54 mS/cm) over a wide temperature range (-90 to +70 °C), owing to the formation of a solvation structure dominated by DEC that weakens the overall coordination interactions between Li$^+$ and solvents. Further optimization can be achieved by tailoring the fluorination degree and fluoride site of the cosolvent. Specifically, the higher fluorination degree and/or the more fluorinated site on the ester

102     group, the weaker interaction between $Li^+$ and solvents, and thus the better low-

103     temperature performance. Consequently 4.5V graphite-based pouch cells (1 Ah)

104     perform stably over 200 cycles under -10 ℃ with only 2% capacity loss and minimal

105     lithium dendrite formation. Even at the ultralow temperature of -70 ℃,

106     NCM811/Graphite and LCO/Graphite pouch cells utilizing the designed electrolytes

107     retained capacity of 716 mAh and 661 mAh, corresponding to 61% and 59% of that at

108     room temperature, respectively. Moreover, these cells could still power electric fans at

109     temperatures as low as -100 ℃. (**Movie S1**).

**Physical properties under extreme low temperature**

111     ETFB, EHFB, and TFEB are all fluorinated derivatives of EB (**Fig S3a**). EB is a

112     suitable co-solvent for LIB electrolytes because of its low melting point (~-100.8 ℃),

113     and its long-alkyl chain, which promotes the formation of a SEI with more favorable

114     properties than those derived from carboxylate solvents with shorter alkyl chains[33]. As

115     expected, all three of the fluorinated derivatives exhibit a lower electron density around

116     the carbonyl O atoms than either EC or EB (**Fig 1a, Table S1**), resulting in weaker

117     binding with $Li^+$ (**Fig 2b & Fig S3b- S4b**). Moreover, the higher fluorination degree of

118     cosolvents, the less electronegative they are, and thus the weaker coordination

119     interaction between $Li^+$ and solvents (**Fig 2b**), evidenced by the lowest binding energy

120     value of EHFB-$Li^+$ (~1.72 eV) and EC-$Li^+$ in EHFB systems (0.71 eV). And the

121     estimated freezing points of the electrolytes evolves in the same trend at that of EC-$Li^+$

122     binding energy, with an increase in the order of EHFB (-135 ℃), TFEB (-132 ℃), and

123     ETFB (-130 ℃) (**Fig. 2d**). Specifically, the EHFB-containing electrolyte exhibited no

124     apparent solidification even when immersed in a -110 ℃ bath for 30 minutes (**Fig. 2e**

125     **& Fig. S5**), and delivers a record-high ionic conductivity of ~1.46 mS/cm even at -90℃

126     (**Fig. 2c**) (**Table S3**) compared to the top LT ion conductivity reported so far[4],

127     demonstrating its great feasibility under extreme cold environment. The temperature-

128     dependence of the conductivity of the cosolvent-containing electrolytes was well

129     described by the empirical Vogel-Fulcher-Tammann (VFT) equation (**Fig S6**), and the

calculated activation energy for EHFB electrolytes was 0.98 eV, much smaller than that of the other four electrolytes (19.19 eV, 2.98 eV, 1.40 eV and 1.41 eV for base, EB, ETFB and TFEB, respectively), further indicative of the great priority of EHFB. In contrast, the base electrolyte began to freeze at about -50 ℃ (**Fig. 2d**) and exhibited poor ionic conductivity when temperature decreases to -90 ℃ (0.001 mS/cm) (**Fig. 2c**).
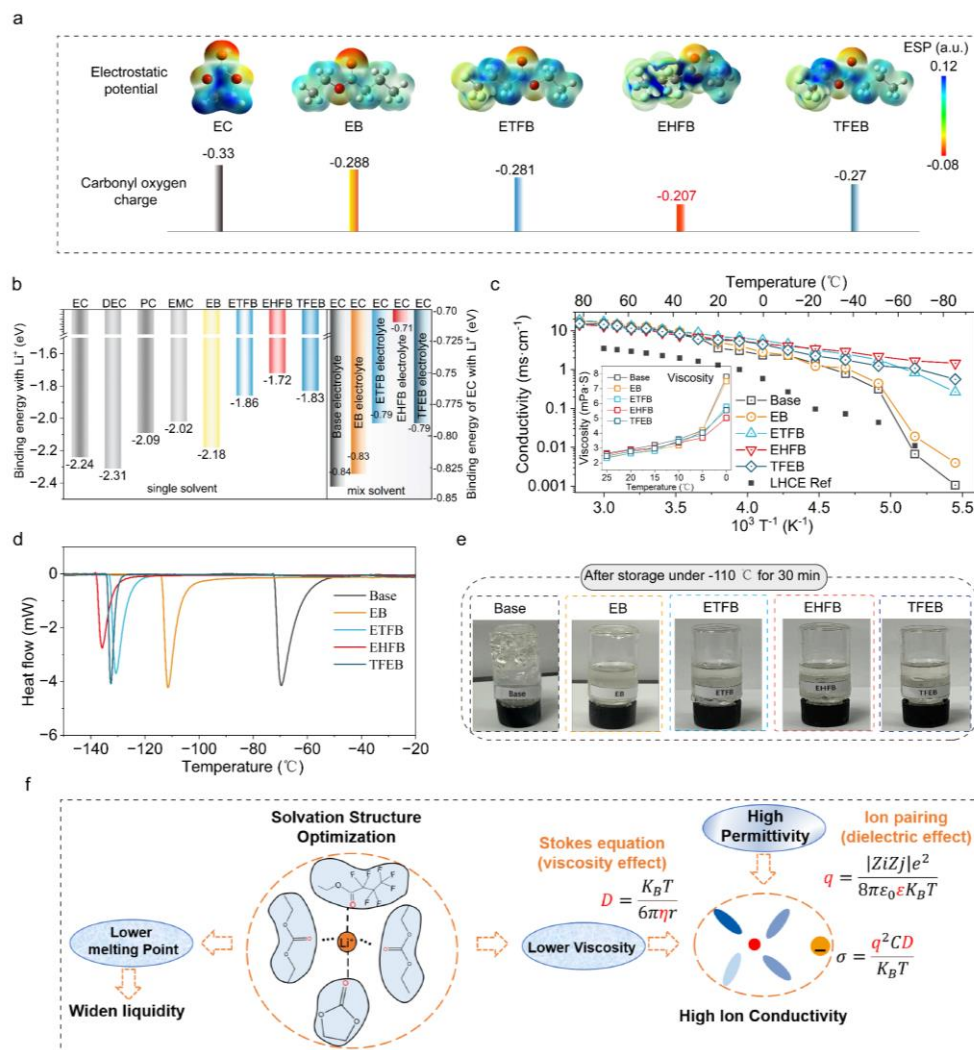


**Fig. 2: a, Electrostatic potential (ESP) maps showing the charge distributions of the solvent molecules considered in this work. b, Binding energies of Li$^+$ with different solvents. c, Conductivity of the base electrolytes and the electrolytes containing EB, ETFB, EHFB, and TFEB. d, DSC curves of the above electrolytes. e, Digital images of different electrolytes after storage at -110 ℃ for 30 minutes. f, Relationship of solvation structure and physical properties of electrolyte.**

The significant improvement in both ion conductivity and liquidity is highly likely due to a change in the solvation structure. This relationship between physical properties and solvation structure is illustrated in **Fig. 2f**. The fluorination weakens the interaction between EC and Li$^+$, evidenced by the lowest EC-Li$^+$ binding energy value in the EHFB

145  system (0.71eV) in the mix solvents (**Fig. 2b**), herein some of EC molecules are

146  released, and the high melting of EC would be compromised by the very low melting

147  of cosolvent in the mixture liquid according to the chemical potential equilibrium theory,

148  leading to a decrease in the melting point and lower viscosity (the inserted figure in **Fig**

149  **2c**) of the bulk electrolyte. Additionally, the ion diffusivity is governed by dielectric

150  effect and viscosity effect[2] (as described in stokes equations in **Fig. 2f**, more details

151  can be found in supporting information of eq.1-eq.3), thus relating the intrinsic nature

152  of conductivity. Therefore, the solvation structure optimization with our strategy can be

153  used to solve both ion conductivity and fluidity issues, which are typically problematic

154  at low temperature. Further solvation structure analysis will be discussed in the

155  following section.

156  **Unlock the electrolyte solvation interaction**

157  The solvation structures were decoupled by performing molecular dynamic (MD)

158  simulations (**Fig S7**) and calculating the radial distribution functions (RDF) (g(r)) and

159  coordination numbers (n(r)) of $Li^+$ in each case (**Fig 3a-b & Fig S8**). In general, the

160  dominant g(r) peak for each solvent appeared at ~2.65 Å, corresponding to the radius

161  of the first solvation shell, while the dominant peak of the Li-P ($PF_6^-$) RDF appears at

162  ~4.2 Å. This means that the $PF_6^-$ anions occupy the second solvation shell, and $Li^+$ and

163  $PF_6^-$ generally exist in the form of separated ion pairs (SIP- $PF_6^-$) rather than being in

164  direct contact. In the base electrolyte, EC is the dominant solvent in the first $Li^+$

165  solvation shell, with a coordination number of 1.31 at room temperature (RT 298K),

166  followed by linear carbonate DEC (1.13) and EMC (0.94), respectively (**Fig 3g & Fig**

167  **S8, Table S6**). The addition of a cosolvent significantly changed the $Li^+$ solvation

168  structure, specifically, EC coordination number was sharply reduced to 0.61 (**Fig 3b &**

169  **3g**) in the EHFB electrolyte, while the DEC coordination number increased to 1.46 (**Fig**

170  **3b & 3g**). Similar trends were observed in the EB, ETFB, and TFEB systems, indicating

171  a transition from an EC-dominant solvation structure to a DEC-dominant one. This

172  transition was found to be fluorination-dependent, and the higher fluorination degree of

173  cosolvent, the stronger coordination of low-ε solvents to $Li^+$ while weakening that of

174  EC. This contributes to overall weak interactions between $Li^+$ and the solvents in

175  electrolyte, and thus facilitate $Li^+$ desolvation and improve LT performance. These

176  effects became more pronounced at lower temperatures. For instance, the DEC

177  coordination number in the EHFB electrolyte increased from 1.46 at 298K to 1.71 at

178  203K, while the EC coordination number fell to 0.33 (from 0.61 at 298K) (**Fig 3h, Fig**

179  **S9, Table S6**), indicating much more EC was replaced by DEC in the first solvation

180  shell at LT. This feature is no doubt favorable for LT applications. In contrast, more EC

181  in the base electrolyte take part in coordination with $Li^+$ upon decreasing temperature,

182  manifested by the increase in the EC coordination number (from 1.34 at 298K to 1.76

183  at 203K) and the reduce in the DEC coordination number (from 1.13 at 298K to 0.74 at

184  203K). Notably, the coordination of PC (which has a similar high-ε with EC) is found

185  no obvious change when introducing cosolvent, this is properly due to PC is much less

186  coordinated competitive with EC.

187  This difference is further verified by the FTIR and Raman spectra analysis under

188  different temperatures (see **Fig 3c-f** and the full spectra presented in **Fig S10** and **Fig**

189  **S11**). In which the free and solvated C=O peaks (in the region of 1660-1870 $cm^{-1}$) were

190  fitted using Voigt functions[27](**Fig 3d, Fig S12-S16**). The peak assignment is presented

191  in supporting information (**Table S7** and **Table S8**). Ratios of solvated to free EC ($R_1$)

192  and solvated EC to solvated DEC ($R_2$) calculated using eq. 1 and eq. 2 were used to

193  quantify the relative abundance of solvated EC as well as the evolution of competence

194  degree for coordination sites between EC and DEC[27].

$$R_1 = \frac{A_{solvated\ EC}}{A_{free\ EC}} \qquad (eq.1)$$

$$R_2 = \frac{A_{solvated\ EC}}{A_{solvated\ DEC}} \qquad (eq.2)$$

197  Here, $A_{solvated\ EC}$, $A_{free\ EC}$ and $A_{solvated\ DEC}$ are the integrated area intensities of the

198  vibrational bands corresponding to solvated and free EC C=O groups and the C=O

199  group of solvated DEC, respectively (**Fig 3d**). Quantitative analysis revealed that both

200  $R_1$ and $R_2$ values decrease upon with decreasing temperature from 298K to 203K (Fig

201    3i), upon the introduce of co-solvent. For instance, $R_1$ value for EHFB electrolyte

202    reduce from 1.34 (at 298K) to 1.09 (at 203K), concurrently with the reduce of $R_2$ from

203    1.53 (at 298K) to 0.66 (at 203K) (**Fig 3i, Table S8**). This trend clearly illustrates that

204    the cosolvent promotes coordination between DEC and $Li^+$, accompanying with

205    weaken interaction between EC and $Li^+$ especially at LT, and thus leading to the first

206    solvation shell structure evolution from being EC-dominant to DEC-dominant. Note

207    that $R_2$ value decreases faster for EHFB electrolyte than ETFB and TFEB (**Fig 3i, Table**

208    **S8**), indicative of its greater selectivity on tailoring DEC-dominant solvation structure

209    at LT. Conversely, for the base electrolyte, both $R_1$ and $R_2$ increase from RT to 203K,

210    corroborates its characteristics of EC-dominant solvation over the wide temperature

211    range (**Fig 3i**). Furthermore, this change was accompanied by a significant blue shift of

212    both two solvated EC peaks in Raman spectra (741 to 749 $cm^{-1}$ and 904 to 911 $cm^{-1}$)

213    with respect to EHFB electrolyte (**Fig 3e, Fig S18**), further indicating that the

214    coordinative interaction between $Li^+$ and EC is much stronger in the base electrolyte at

215    $LT^{[16, 23]}$. This impedes its practical utility under cold conditions. These aforementioned

216    features in terms of reduced $R_1$ and $R_2$ values, suppressed blue shift of C-O band (**Fig**

217    **3f**) well support hypothesis that cosolvents bearing strongly electron-withdrawing

218    fluorinated groups efficiently promote the coordination of weakly polar linear

219    carbonate solvents (i.e., DEC) to $Li^+$ while suppressing that of more polar cyclic

220    carbonates (i.e., EC), especially at LT (**Fig 3j**), consisting well with the RDFs derived

221    from the MD simulations (**Fig 3a**). Moreover, the fluorinated cosolvent itself also

222    contributes to $Li^+$ solvation, and the corresponding coordination numbers (in primary

223    solvation shell at RT are estimated to be 1.3 for EB, 0.85 for ETFB, 0.06 for EHFB,

224    and 0.74 for TFEB, decrease with the increase of fluorination degree (**Fig 3g & Fig S8,**

225    **Table S6**). These results agree well with the calculated binding energies of $Li^+$ with

226    solvents shown in **Fig 2b**. Interestingly, EHFB trends to coordinate with $Li^+$ at LT

227    although its lowest coordination behavior at RT, manifested by the temperature related

228    coordination number drastically increasing from 0.06 at 298K to 0.56 at 203K (**Fig 3h**).

229    This indicates that the coordination ability of EHFB molecular was auto-activated under

230    LT, and more cosolvent taking part in the solvation process. The low-ε solvent dominant

solvation structure combining with the cosolvent participating in, ultimately and radically contribute to overall weaken interactions between $Li^+$ and the coordinated solvents in the inner solvation sheath (**Fig 3j**). These features are favorable for facilitating $Li^+$ desolvation, and no doubt promote electrochemical kinetics at LT.
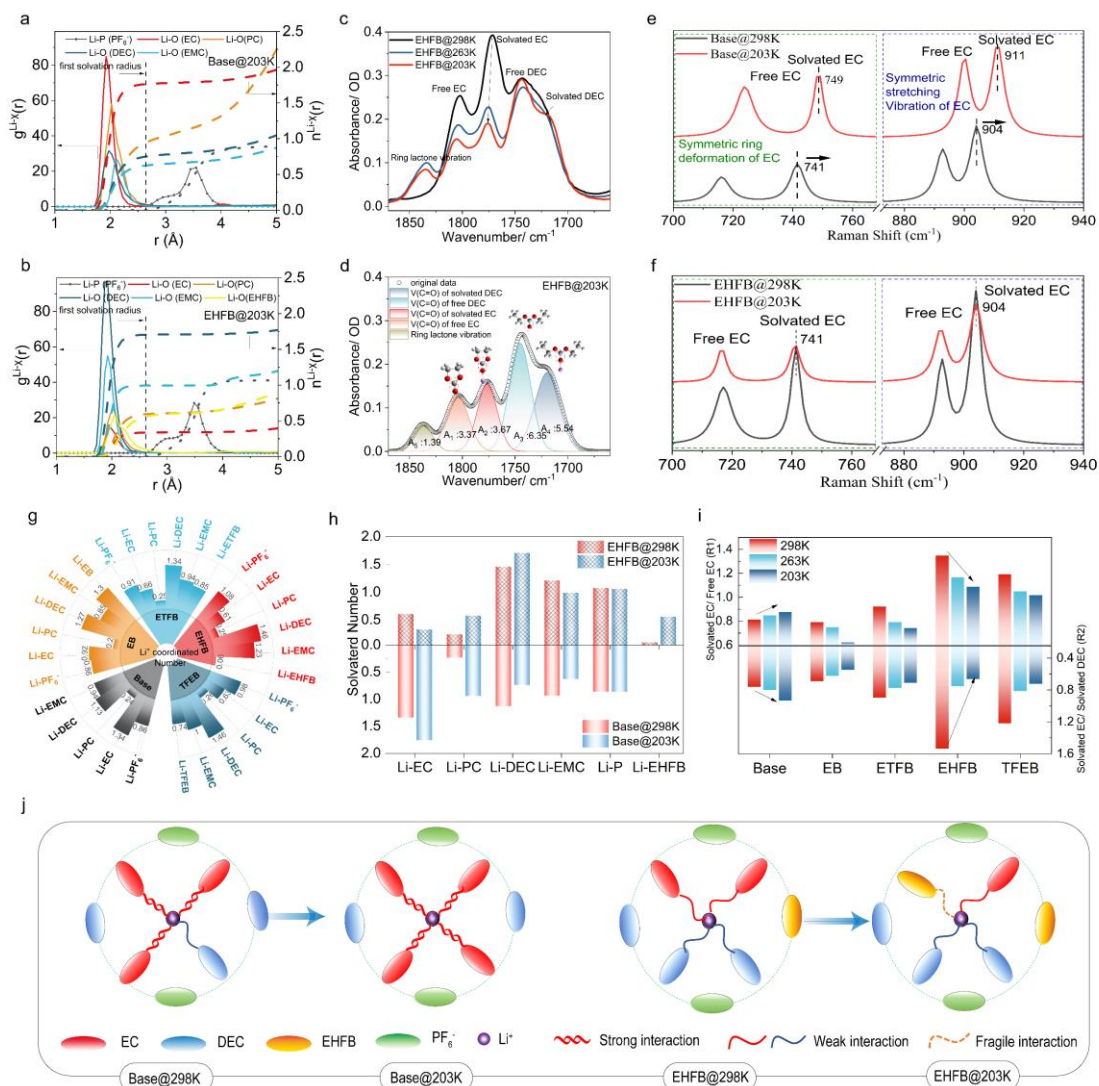


**Fig. 3: Calculated radial distribution functions (g(r)) and coordination numbers (n(r)) at 203K for the base electrolyte (a) and the EHFB electrolyte (b) based on molecular dynamics (MD) simulations. c, The C=O regions of the FTIR spectra of EC and DEC in the EHFB electrolyte at different temperatures. d, Fitting spectra with Voigt function for the EHFB electrolyte of 203K. Raman spectra for symmetric ring deformation of EC and stretching vibration of the C-O bond in the base electrolyte (e) and the EHFB electrolyte (f). g, Coordination numbers for the five studied electrolytes at 298K based on the calculated RDFs. h, Coordination numbers of all solvent components with $Li^+$ in the base and EHFB electrolytes at 298K and 203K. i, Ratios of solvated EC to free EC, and solvated EC to solvated DEC in the base and EHFB electrolytes (derived from FTIR spectra) at different temperatures. J, Illustration of solvation structure changes in the base and EHFB electrolytes upon lowering the temperature from 298K to 203K.**

## Promotion of Li$^+$ desolvation and improvement of electrochemical kinetics

DFT calculations reveal that introducing the fluorinated cosolvent EHFB dramatically reduced the Li$^+$ desolvation energy for a simplified EC/DEC electrolyte from ~-1.1 eV to ~-0.84 eV (**Fig 4a**). Moreover, the higher fluorination degree of the cosolvent, the smaller desolvation energy. This is attributed to the strongly electron-withdrawing effects of fluorine substituents that efficiently promotes the coordination between Li$^+$ and low-$\varepsilon$ solvents, and forming DEC dominated solvation structure with overall reduced interactions between Li$^+$ and solvents (**Fig 4b**), thereby facilitating desolvation process (**Fig 4b**).

Further evidences of the impact of the fluorinated cosolvent on Li$^+$ desolvation are derived from the distribution of relaxation times (DRT) analysis (for details, see the supporting information) (**Fig 4c-d**)[34, 35, 36]. In which different electrochemical process are classified via a local maximum in a continuous distribution function[37, 38, 39]. Specifically, the DRT peak at low frequency ($10^1 > \tau > 10^{-1}$) was assigned to charge transfer resistance ($R_{ct}$), the intermediate frequency peak ($10^{-1} > \tau > 10^{-3}$) was attributed to the resistance that lithium-ion transport through the SEI ($R_{SEI}$), and the high frequency peak ($10^{-3} > \tau > 10^{-4}$) was identified as the contact resistance ($R_0$), in accordance with the literature[34]. Both $R_{ct}$ and $R_{SEI}$ were found to be highly temperature-dependent, $R_{ct}$ is dominant at low temperature, whileas, $R_{SEI}$ is found to be dominant at high temperature (**Fig S20**), consisting with previous reports[36]. $R_{ct}$ in the EHFB electrolyte was determined to be 1.0 $\Omega$ at -60 °C (**Fig 4d**), followed with 4.7 $\Omega$ for ETFB, and 3.2 $\Omega$ for TFEB (**Fig S19 - Fig S21**). All these values are much smaller than that of the base electrolyte (8.8 $\Omega$) (**Fig 4c**), highlighting the important role of cosolvents in facilitating charger transfer. This is also verified by the reduced activation energies of charge transfer in **Fig 4f**. In which, the value is estimated to be 10.9 kJ/mol for LCO/Gr pouch cell with the EHFB electrolyte, which is about one third of that in base electrolyte (30.4 kJ/mol). And the activation energy increases in the order of EHFB, TFEB, and ETFB, agreeing well with the evolution trend of desolvation energy in **Fig. 4a**. The sluggish kinetics in the graphite anode part is reported to be the main challenge

276     that will push the $Li^+$ intercalation potential into graphite below 0 V (vs. $Li/Li^+$)[8, 9, 25,

277     30], which is verified by the much larger impedance of the graphite anode compared to

278     the LCO cathode, especially at LT (**Fig S22**). DRT mapping of Gr/Li half-cells over

279     two electrochemical cycles at -10 ℃ in the base and EHFB electrolytes (**Fig 4g-h**)

280     reveal that, the EHFB system exhibit much smaller $R_{ct}$ compared with the base

281     electrolyte, again implying that the cosolvent can facilitate charger transfer for the low

282     temperature trapped graphite anode. In addition, significant decreased $R_{SEI}$ in the in-

283     situ electrochemical process (**Fig 4g-h**) was also observed, which implied that the

284     cosolvent also works for $Li^+$ transport through the SEI. This is evidenced by the much

285     smaller activation energy of $Li^+$ transport through the SEI in full cells with EHFB (19.8

286     kJ/mol) compared with that in the base electrolyte (29.3 kJ/mol) (**Fig 4e**). Meanwhile,

287     $R_{SEI}$ increased during initial charging and then declined during the subsequent

288     electrochemical operations (**Fig 4g**), suggesting that SEI derived from the base

289     electrolyte is comparatively unstable and poorly conductive[40]. Conversely, in the EHFB

290     system, the $R_{SEI}$ was smaller and more stable (**Fig 4h**). The significantly decreased

291     activation energy and lower resistance of this graphite/Li cell could be attributed to

292     formation of a thin, inorganic-rich fluorine-containing SEI derived from the fluorinated

293     cosolvent, as reported previously[41] and illustrated in the following discussion.

294
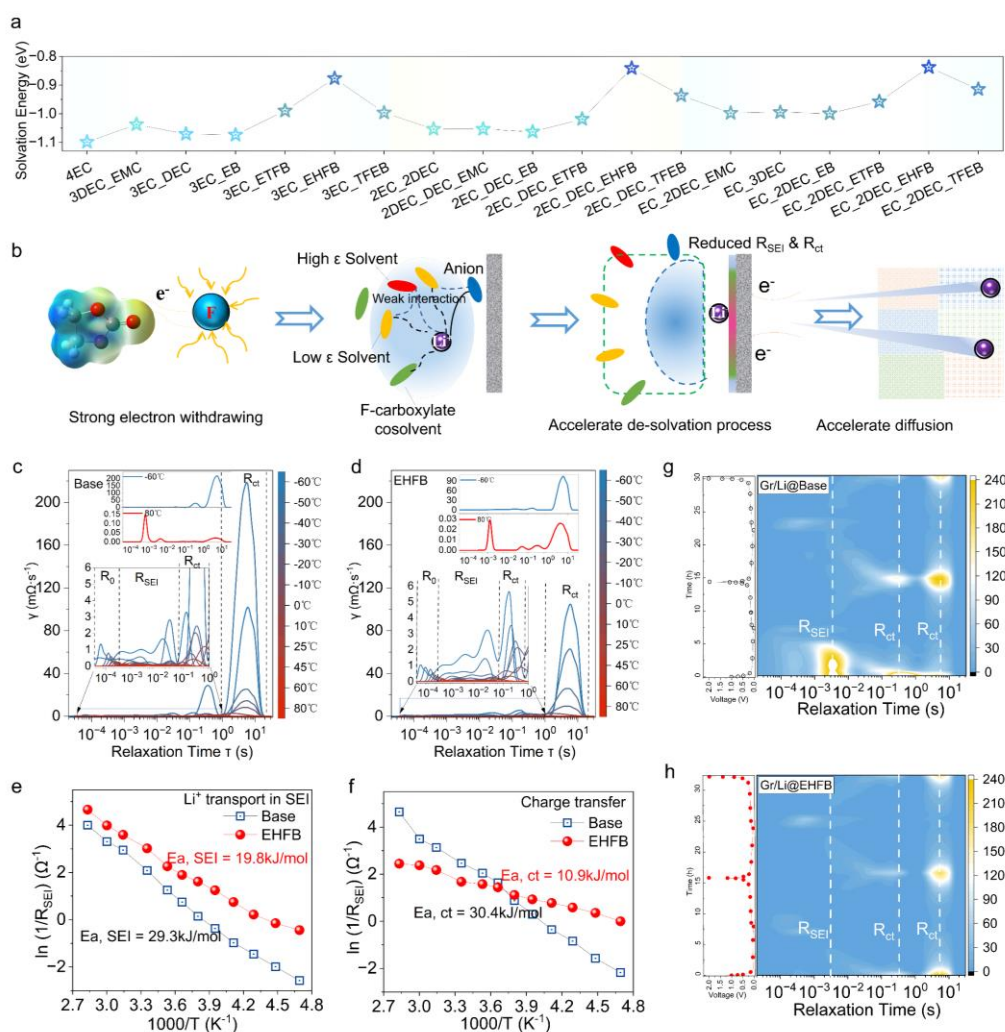
**Fig. 4: Desolvation behavior and its effect on electrochemical kinetics.** a, Li$^+$ solvation/desolvation energies in different electrolytes. b, Illustration of fluorinated co-solvent's key role in weakening the interactions between Li$^+$ and solvent molecules, accelerating desolvation and facilitating Li$^+$ diffusion. Temperature-dependent distribution of relaxation times (DRT) plot derived from EIS data for the base electrolyte (c) and the EHFB electrolyte in LCO/Gr pouch cells (d). Corresponding activation energies derived by Arrhenius fitting for R$_{ct}$ (e) and R$_{SEI}$ (f) with the base and EHFB electrolytes. In-situ DRT data representing two cycles of graphite/Li half-cells with the base electrolyte (g) and the EHFB electrolyte (h) at 263K.

303

## Role of the solvation structure toward SEI properties

305       The SEI compositions and structural evolutions on the cycled graphite electrodes

306 were characterized by time-of-flight secondary ion mass spectrometry (TOF-SIMS).

307 The depth profiles of TOF-SIMS showed that organic moieties (CH$_2^-$, CO$_3^-$, C$_2$H$_3$O$^-$,

308 and C$_2$H$_3$O$_2^-$) were mainly concentrated on the outface of SEI (**Fig 5c-d & Fig S28**),

309 while inorganic LiF species (LiF$_2^-$, Li$_2$F$_3^-$, Li$_3$F$_4^-$, Li$_4$F$_5^-$) and OH$^-$ became more

310      prevalent at the inner side of SEI (**Fig 5a-b, Fig S27**), agreeing well with previously

311      reported SEI distribution[42, 43, 44]. **Table S9** listed the attribution of the fragment ions and

312      their potential sources, including three organic components: $ROCO_2Li$ (representing

313      $CO_3^-$ fragment), $CH_3COLi$ ($C_2H_3O^-$) and $CH_3COOLi$ ($C_2H_3O_2^-$), which were produced

314      through the electrochemical reduction of EC, DEC and carboxylate, respectively. When

315      temperature decreased from 298K to 263K, the $ROCO_2Li$ signal was strengthened (**Fig**

316      **5c & Fig S29a**) while $CH_3COLi$ signal was weakened (**Fig 29b**) and almost no

317      $CH_3COOLi$ signal was detectable in base electrolyte (**Fig 5d & Fig S29c**). This directly

318      indicates severe reduction of EC at LT while that of DEC became insignificant.

319      Conversely, upon cooling to 263 K, the $ROCO_2Li$ signal was weakened and the

320      $CH_3COLi$ signal became stronger when using the EHFB electrolyte, (**Fig 5c, Fig S29**),

321      implying intensified DEC reduction decomposition with EHFB contained at LT while

322      the decomposition of EC declined. This is well consistent with the previously discussed

323      results (**Fig 3g-k**) that the solvation of $Li^+$ by EC is promoted at LT when using the base

324      electrolyte but is inhibited when using EHFB electrolyte, while the opposite trend is

325      observed for DEC. In addition, detectable $CH_3COOLi$ signal suggests that the

326      fluorinated cosolvent contributes to the solvation structure and participates in film

327      forming on the graphite surface at LT (**Fig 5d**), agreeing well with the calculation result

328      of LUMO energies (**Table S2**). More LiF species in the interface derived from EHFB

329      is much higher than that in base electrolyte at the same LT (**Fig 5a-b**) and increased as

330      the temperature decreased (**Fig S27c-d**). These differences are manifested in the 3D

331      spatial distributions overlay of organic SEI components ($C_2H$, $ROCO_2Li$) and inorganic

332      species (LiF, $Li_2O$) under different temperature conditions (**Fig 5g**). The organic

333      component (i.e. $C_2H$) was found only in the outermost layer of SEI with low contents

334      for EHFB cases, while more LiF were identified throughout the underlying layers and

335      increase from 0.029 to 0.042 a.u. with lowering temperature, properly benefited from

336      more EHFB-participated solvation structure as proven in **Fig 3h**. In contrast, the base

337      electrolyte-derived SEI delivers much smaller amount of LiF species (**Fig 5a, Fig 5d**).

338      These "Friendly" anionic components are highly conductive interface species[42, 45]. The

339      detailed mass spectra and 3D distributions are represented in **Figure S24-26** and **Fig**

340  **S31**, respectively. In addition, the dissolution of $Co^+$ was captured in the graphite anode

341  cycled with base electrolyte which is known to be highly destructive for SEI[46], while it

342  was almost undetectable with EHFB electrolyte (**Fig 5e-f & Fig S30a-d**). This is

343  possibly due to the oxidation resistance of fluorination, which can be verified by the

344  LSV result (**Fig S41**), highlighting the significant advantages of fluorination cosolvent

345  toward high voltage applications and the excellent performance of SEI distributions of

346  this kind with EHFB cosolvent. All these together, rightly explained the superior

347  desolvation kinetic and LT performance observed in the EHFB electrolyte (**Fig 4c-h**).



348
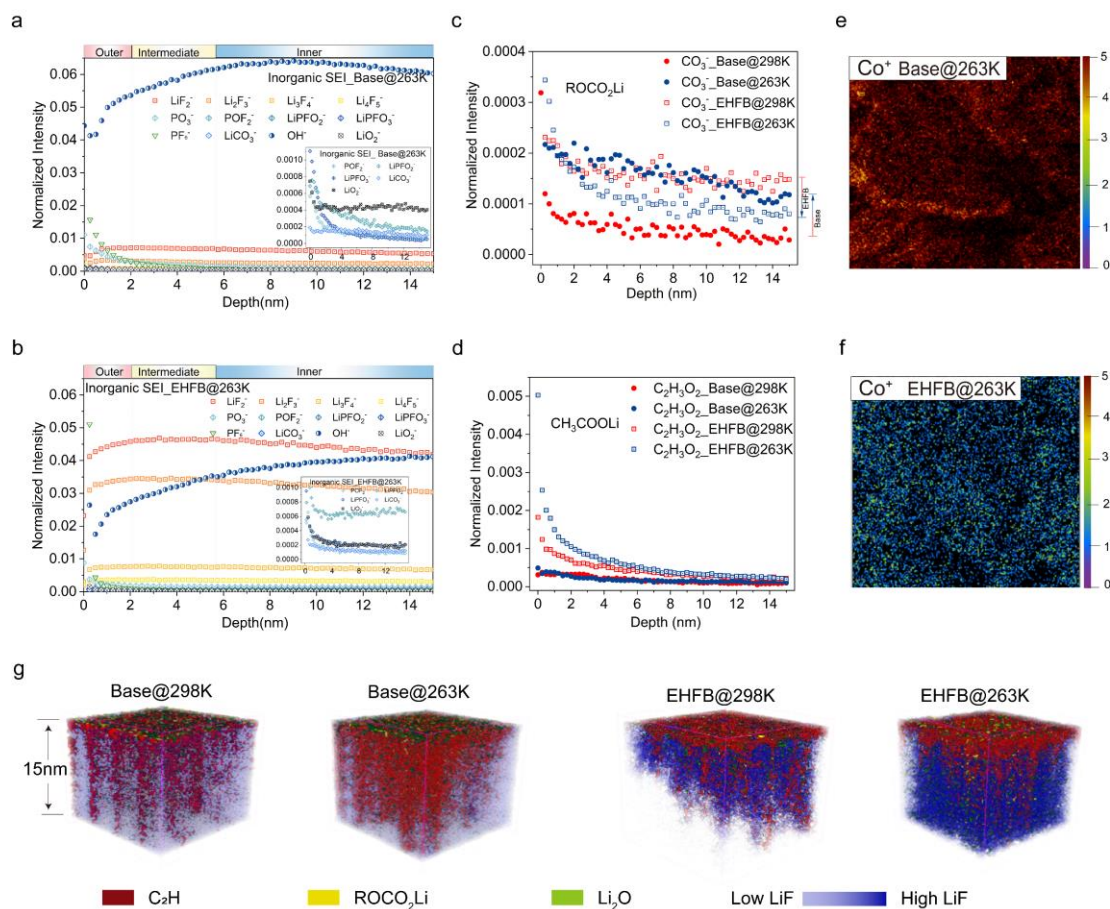
349  **Fig. 5: TOF-SIMS characterization of the features and structural evolution of SEI at the graphite**
350  **anode.** Depth profiles of functional groups in the inorganic SEI after prolonged cycling at 263K for the
351  base electrolyte (a) and the EHFB electrolyte (b). Depth profiles of the $ROCO_2Li$ component (c) and
352  $CH_3COOLi$ component (d) in the SEI formed from the base and EHFB electrolytes at 298K and 263K.
353  The spatial distribution of $Co^+$ on the graphite anode for the base electrolyte (e) and EHFB electrolyte
354  (f). g, 3D reconstructions of the topmost 15nm of the graphite anode SEI formed at 298K and 263K for
355  the base electrolyte and EHFB electrolyte cells.

**Comparative electrochemical performance at low temperature.**

Coupling EHFB electrolyte with commercial NCM811/Gr (1 Ah) and LCO/Gr pouch cells (1 Ah) yielded excellent electrochemical performances especially at LT, as demonstrated by capacity retention of up to 97.94% and 86.70%, respectively, after 200 cycles at -10°C with a cut-off potential of 4.5V (**Fig 6a-b**). Furthermore, LCO/Gr pouch cells with EHFB electrolyte retained a high capacity of 830 mAh at -40 °C, corresponding to 73.9% of their RT capacity (**Fig 6d**). Notably, these cells retained ~60% of their RT capacity at even -70 °C (**Fig 6d**), and could even power an electric fan at -98.4 °C (**Fig 6h, Fig S40, Movie S1 & S2**), demonstrating the viability of the new electrolyte at extremely low temperatures. Usable battery performance was thus achieved at temperatures below the condensation point of $CO_2$ (-78 °C), demonstrating the remarkable low-temperature performance of the EHFB electrolyte. Similar excellent performance was achieved in NCM811/Gr pouch cells, which retained 61% of their RT capacity at -70 °C (**Fig S36**). In contrast, cells using the base electrolyte exhibited significantly lower performance, retaining only 79.4% of their RT capacity at -10°C, and were totally failed at -40°C (**Fig 6c**).

Considering the much concerned issue of lithium dendrite formation at LT[47], the differential voltage profiles of cells with the two electrolytes were thereby compared to evaluate the extent of lithium plating[47]. A much more pronounced Li plating peak was observed for cells using the base electrolyte compared to those with EHFB (**Fig 6f**). And the yellow deposits of metallic Li were clearly identified on the surface of the base electrolyte -cycled graphite anode under -10 °C (**Fig 6g & Fig S38**), but not on those from cells using the EHFB electrolyte. These findings were consistent with optical images acquired using a TOF-SIMS camera (**Fig S23**) and SEM images of the cycled graphite (**Fig S39**), and further supports are derived from the low temperature performance comparation between graphite and metallic lithium anode (**Fig S33**). The Gr/Li cells with the EHFB electrolyte retained 57% and 95% of their RT capacity at -70 °C and -20 °C, respectively, which are much higher than those in the base electrolyte (20% and 69%, respectively, **Fig 6e**). In addition, Gr/Li cells using electrolytes

containing fluorinated cosolvents (especially EHFB) exhibited very stable cycling performance over 120 cycles with 99% capacity retention under -10 °C (**Fig S37c**), whileas the Gr/Li cells coupled with base electrolyte exhibits dramatic capacity loss within the first 20 cycles (from 249.3 to 28.5 mAh/g), followed by a slow increase in capacity that ultimately stabilized at 100 mAh/g after 120 cycles (**Fig S37c**). This poor cycling behavior in base electrolyte is attributed to the insufficient lithiation at LT resulting from the accumulation of lithium dendrites. All these, together, further corroborate fluorination carboxylate cosolvent-contained electrolyte is highly compatible with the graphite anode. This significantly improves the practicality of graphite-based cell when operating in cold conditions.
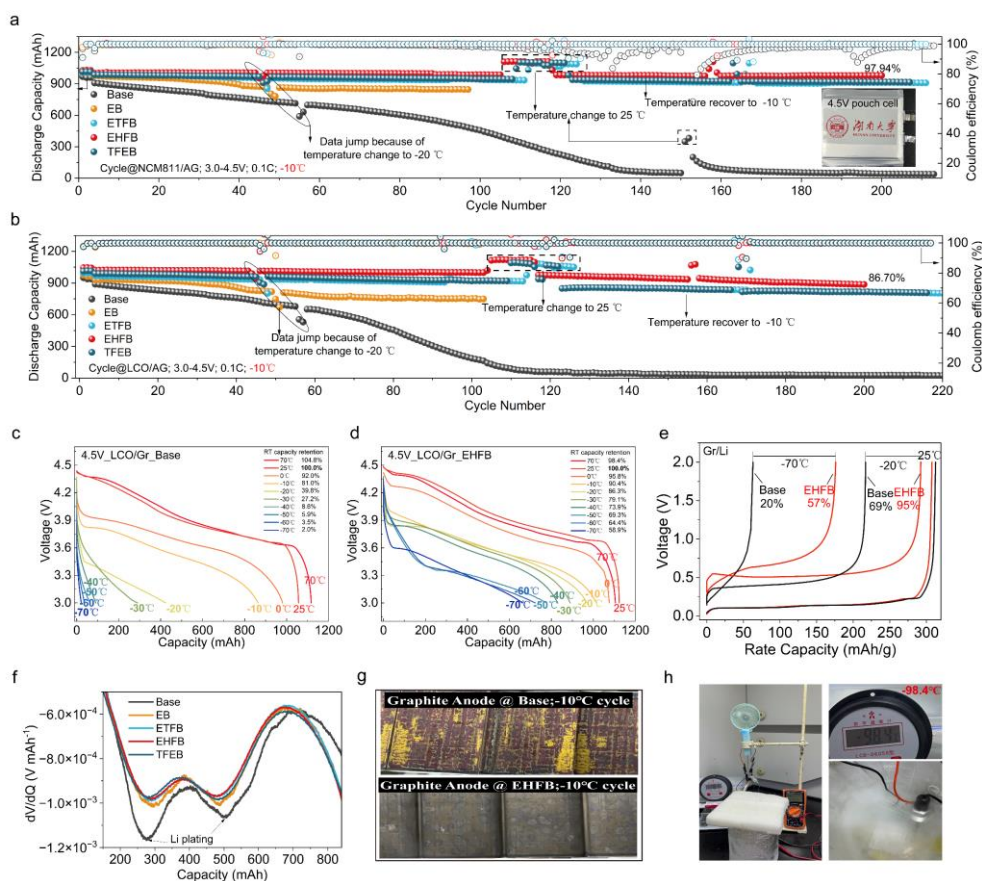


**Fig. 6: Low temperature performance of the commercial LiCoO₂/Graphite (LCO/Gr) and LiNi₀.₃Co₀.₃Mn₀.₃O₂/Graphite (NCM811/Gr) pouch cell with the designed electrolytes and common electrolyte.** a-b, Cycling behavior of NCM811/Gr cell (a) and LCO/Gr (b) with different electrolyte under -10℃. c-d, The temperature-dependent discharge profiles of LCO/Gr pouch cells with Base electrolyte (c) and EHFB electrolyte (d). e, Charge profiles of Gr/Li cells with different electrolyte at different temperature. f, Differential voltage (dV/dQ) profiles of the 100th discharge curve cycled at -10℃. g, Optical images of the dismantled graphite after the long cycling at low temperature. h, Optical images of an electric fan powered by the 4.5V LCO/Gr pouch cell using EHFB electrolyte at superior low temperature -98.4℃. The video is in supporting information (Movie S1 and S2).

405    Additionally, the best rate performance of Gr/Li was achieved with EHFB

406    electrolyte (**Fig S37a**), retaining 77.7 mAh/g at 5C and subsequently recovering

407    immediately to its initial capacity with 331.6 mAh/g at 0.2C. All these demonstrates

408    that it could be extended for the fast charge applications, considering there are some

409    common issues with graphite anode operation at low temperature and high C-rates.

410    Furthermore, the corresponding room temperature and high temperature cycling

411    performance of the pouch cells and Gr/Li cells (**Fig S34-Fig S35**) showed that the

412    cosolvents contained cells behaved much better than those without, with 800mAh/g

413    retained at the $55_{th}$ cycle under 60 °C, and negligible capacity loss within the 100 cycles

414    at 25 °C for NCM811/Gr cells. All these, verified the feasibility that cells containing

415    the proposed cosolvent could operate for all the temperatures.

416    **Conclusion**

417    Regulating the electronegativity of carbonyl oxygen of EC via introducing

418    fluorinated cosolvent weakens the strong coordination of EC to $Li^+$, thus achieved a

419    fluorine-dependent transition from EC-dominated SSIP to DEC-dominated one,

420    especially at low temperatures. As a result, there is an overall weak connection between

421    $Li^+$ and solvent that leading to ease desolvation of $Li^+$, and still maintaining the high

422    dielectric property of EC. Moreover, the cosolvents participated in weak coordination

423    were also easily decomposed to form a fluorine-rich SEI. The designed solvation

424    structure leads to dramatic improvements in low temperatures, which enables wider

425    liquidity (retaining liquid at -110 °C), better conductivity (1.46 mS/cm at -90 °C), and

426    more facilitated desolvation process. These improvements allow 4.5V graphite-based

427    pouch cells to maintain stable operation over 200 cycles at -10 °C with only 2% capacity

428    loss and no detectable lithium dendrite formation. Additionally, the cells can operate at

429    -70 °C while retaining 60% of their room temperature capacity and can power electrical

430    devices at extremely low temperatures of ~ -100°C. Overall, this solvation design

431    strategy in traditional EC-based electrolytes provides a unique approach to develop

432    lithium-ion batteries suitable for use in extreme environments.

## Methods

### Electrolyte preparation and battery fabrication.

The base electrolyte was prepared by dissolving 1M $LiPF_6$ in a mixture of carbonate solvents (EC: PC: DEC: EMC = 2:1:3:4 by volume). Test electrolytes were prepared with the same concentration of $LiPF_6$ but with half of the DEC replaced with a fluorinated cosolvent or EB, giving a solvent composition of EC: PC: DEC: EMC: cosolvent = 2: 1: 1.5: 4: 1.5 by volume. Four cosolvents were tested: EB and its fluorinated analogs ETFB, EHFB, and TFEB.

1Ah dry pouch cells obtained from Li-Fun Technology were injected with 4.3g of electrolyte for NCM811/Gr cells or 2.1g for LCO/Gr cells in a glovebox filled with argon. The standard cell formation process was then completed by performing gas release and re-sealing to obtain cells with an electrochemical window of 3-4.5V.

### Electrochemical measurements

The charge/discharge behaviors of the batteries (coin cells and pouch cells) were tested using a battery test system (CT-4008T-5V6A, CT-4008T-5V10mA, Neware, Shenzhen, China). Batteries to be tested were placed in the chamber (GMC-71, Espec, Guangzhou, China) and brought to an appropriate onset temperature for the desired test. Electrical impedance spectroscopy was performed over a frequency range from 0.01 Hz to 100K Hz on an electrochemical work station (Solartron 1455A, Solartron Group, UK) with an amplitude of 10 mV.

### Electrolyte characteristic

The conductivity of the electrolytes was determined with a conductivity meter (Mettler Toledo, Shanghai, China) in a cold trap containing a mixture of ethyl alcohol and liquid nitrogen whose temperature was adjusted by varying the ratio of the two substances. FTIR spectra were acquired using a Fourier Transform Infrared Spectrometer (Nicolet, iS50 FT-IR, Thermo Scientific, KBr tablet, wave number 4000-600 $cm^{-1}$). Raman spectra were acquired with a WITEC alpha 300R Raman system

460     (532 nm laser, laser power 2mW). The electrolyte was storage at the onset temperature

461     with the same temperature controlling device of conductivity before FTIR and Raman

462     test.

463     **TOF-SIMS**

464     Chemical mapping and depth profile analyses of anode samples were conducted

465     using a TOF-SIMS instrument (PHI nano TOF II, MN, USA). $Bi^+$ source produced by

466     a 30 KeV bismuth liquid metal ion gun with a DC current of 300pA were used as

467     primary ions for chemical mapping analysis. Positive and negative ion TOF-SIMS

468     images were acquired in unbunched mode from 20 μm by 20 μm areas of each sample

469     with a spatial resolution as low as 70 nm. For spectrum and depth profiles analysis, The

470     $Bi3^{++}$ ions produced by a 30 KeV bismuth liquid metal ion gun with DC current of

471     9.7nA were used as primary ions for spectrum and depth profile analysis. Positive and

472     negative ion TOF-SIMS spectrum were acquired in bunched mode from 150 μm by 150

473     μm areas of each sample with a mass resolution of around 12000 for m/z 28($Si^+$).

474     During depth profiling SEI layers, an Argon ion ($Ar^+$) gun was used for sputtering. The

475     sputtering rate was 5nm/min for standard $SiO_2$. A slow sputtering interval of around

476     0.25 nm for each cycle was used to improve the quality of the depth profile curves.

477     Mass scale calibration was performed using common fragment ions (Positive mode:

478     $CH_3^+$, m/z:15.02; $C_2H_3^+$, m/z:27.02; $C_3H_5^+$, m/z:41.04; Negative mode: $CH^-$, m/z:13.00;

479     $C_2H^-$, m/z:25.00; $C_4H^-$, m/z:49.00). Data processing was performed using PHI TOF-DR

480     software (Physical Electronics, Minnesota, USA).

481     **Computational methods.**

482     Geometry optimization, energy calculations, and electronic structure analyses of

483     electrolyte and solvent molecules were performed using the Gaussian 16 package with

484     the B3LYP functional[48] and the 6-311G(d,p) double-zeta basis set[49]. Frequency

485     analyses were performed using the same basis set to verify the stability of the optimized

486     structures. Solvation effect for the complexes of $Li^+$ with different molecules were

487     evaluated by using the SMD implicit solvation model with acetone (ε=20.49) as the

continuum solvent. Molecule dynamic simulations of the common electrolyte (EC:PC:DEC:EMC=20:10:30:40) and the four cosolvent-containing electrolytes (EC:PC:DEC:EMC:cosolvent=20:10:15:40:15 by volume) were performed using the Forcite module in Material Studio software with the COMPASS III ab initio forcefield [50] and the Nosé thermostat[51]. The numbers of different molecules in the five systems are shown in Table S5. Before performing simulations with the canonical ensemble (NVT) at the specified temperature for 10 ns, the density of each system was equilibrated with the NPT ensemble for tens of picoseconds.

**Acknowledgements**

# Reference

1. Li Q, Liu G, Cheng H, Sun Q, Zhang J, Ming J. Low-Temperature Electrolyte Design for Lithium-Ion Batteries: Prospect and Challenges. *Chemistry – A European Journal* **27**, 15842-15865 (2021).

2. Hou J, Yang M, Wang D, Zhang J. Fundamentals and Challenges of Lithium Ion Batteries at Temperatures between −40 and 60 °C. *Advanced Energy Materials* **10**, 1904152 (2020).

3. Rodrigues M-TF, *et al.* A materials perspective on Li-ion batteries at extreme temperatures. *Nature Energy* **2**, 17108 (2017).

4. Fan X, *et al.* All-temperature batteries enabled by fluorinated electrolytes with non-polar solvents. *Nature Energy* **4**, 882-890 (2019).

5. Jow TR, Delp SA, Allen JL, Jones J-P, Smart MC. Factors Limiting Li+ Charge Transfer Kinetics in Li-Ion Batteries. *Journal of The Electrochemical Society* **165**, A361 (2018).

6. Li Q, *et al.* Li+-Desolvation Dictating Lithium-Ion Battery's Low-Temperature Performances. *ACS Applied Materials & Interfaces* **9**, 42761-42768 (2017).

7. Liao B, *et al.* Designing Low Impedance Interface Films Simultaneously on Anode and Cathode for High Energy Batteries. *Advanced Energy Materials* **8**, 1800802 (2018).

8. Nan B, *et al.* Enhancing Li+ Transport in NMC811||Graphite Lithium-Ion Batteries at Low Temperatures by Using Low-Polarity-Solvent Electrolytes. *Angewandte Chemie International Edition* **61**, e202205967 (2022).

9. Yang Y, *et al.* Synergy of Weakly-Solvated Electrolyte and Optimized Interphase Enables Graphite Anode Charge at Low Temperature. *Angew Chem Int Ed Engl* **61**, e202208345 (2022).

10. Hu D, *et al.* Research Progress of Lithium Plating on Graphite Anode in Lithium-Ion Batteries. *Chinese Journal of Chemistry* **39**, 165-173 (2021).

11. Konz ZM, McShane EJ, McCloskey BD. Detecting the Onset of Lithium Plating and Monitoring Fast Charging Performance with Voltage Relaxation. *ACS Energy Letters* **5**, 1750-1757 (2020).

12. Ren D, *et al.* Investigation of Lithium Plating-Stripping Process in Li-Ion Batteries at Low Temperature Using an Electrochemical Model. *Journal of The Electrochemical Society* **165**, A2167 (2018).

544 13. Senyshyn A, Mühlbauer MJ, Dolotko O, Ehrenberg H. Low-temperature performance of
545 Li-ion batteries: The behavior of lithiated graphite. *Journal of Power Sources* **282**, 235-
546 240 (2015).
547

548 14. Waldmann T, *et al.* Interplay of Operational Parameters on Lithium Deposition in Lithium-
549 Ion Cells: Systematic Measurements with Reconstructed 3-Electrode Pouch Full Cells.
550 *Journal of The Electrochemical Society* **163**, A1232 (2016).
551

552 15. Zhang G, *et al.* Lithium plating on the anode for lithium-ion batteries during long-term
553 low temperature cycling. *Journal of Power Sources* **484**, 229312 (2021).
554

555 16. Dong X, Wang Y-G, Xia Y. Promoting Rechargeable Batteries Operated at Low
556 Temperature. *Accounts of Chemical Research* **54**, 3883-3894 (2021).
557

558 17. Zhu G, *et al.* Materials insights into low-temperature performances of lithium-ion
559 batteries. *Journal of Power Sources* **300**, 29-40 (2015).
560

561 18. Cheng H, *et al.* Emerging Era of Electrolyte Solvation Structure and Interfacial Model in
562 Batteries. *ACS Energy Letters* **7**, 490-513 (2022).
563

564 19. Heiskanen SK, Kim J, Lucht BL. Generation and Evolution of the Solid Electrolyte Interphase
565 of Lithium-Ion Batteries. *Joule* **3**, 2322-2333 (2019).
566

567 20. Rustomji CS, *et al.* Liquefied gas electrolytes for electrochemical energy storage devices.
568 *Science* **356**, eaal4263 (2017).
569

570 21. Yang Y, *et al.* High-Efficiency Lithium-Metal Anode Enabled by Liquefied Gas Electrolytes.
571 *Joule* **3**, 1986-2000 (2019).
572

573 22. Smart MC, Ratnakumar BV, Chin KB, Whitcanack LD. Lithium-Ion Electrolytes Containing
574 Ester Cosolvents for Improved Low Temperature Performance. *Journal of The*
575 *Electrochemical Society* **157**, A1361 (2010).
576

577 23. Dong X, *et al.* High-Energy Rechargeable Metallic Lithium Battery at −70 °C Enabled by
578 a Cosolvent Electrolyte. *Angewandte Chemie International Edition* **58**, 5623-5627 (2019).
579

580 24. Xiao P, Zhao Y, Piao Z, Li B, Zhou G, Cheng H-M. A nonflammable electrolyte for
581 ultrahigh-voltage (4.8 V-class) Li||NCM811 cells with a wide temperature range of 100 °C.
582 *Energy & Environmental Science* **15**, 2435-2444 (2022).
583

584 25. Qin M, *et al.* Rejuvenating Propylene Carbonate-based Electrolyte Through Nonsolvating
585 Interactions for Wide-Temperature Li-ions Batteries. *Advanced Energy Materials* **n/a**,
586 2201801 (2022).

587

588    26.    Piao N, *et al.* Countersolvent Electrolytes for Lithium-Metal Batteries. *Advanced Energy*
589           *Materials* **10**, 1903568 (2020).

590

591    27.    Wu Y, *et al.* Significance of Antisolvents on Solvation Structures Enhancing Interfacial
592           Chemistry in Localized High-Concentration Electrolytes. *ACS Central Science* **8**, 1290-
593           1298 (2022).

594

595    28.    Jin Y, *et al.* Low-solvation electrolytes for high-voltage sodium-ion batteries. *Nature*
596           *Energy* **7**, 718-725 (2022).

597

598    29.    Xu J, *et al.* Electrolyte design for Li-ion batteries under extreme operating conditions.
599           *Nature*, (2023).

600

601    30.    Yang Y, *et al.* Rechargeable LiNi0.65Co0.15Mn0.2O2||Graphite Batteries Operating at −60

602           °C. *Angewandte Chemie International Edition* **61**, e202209619 (2022).

603

604    31.    Zhang Z, *et al.* Fluorinated electrolytes for 5 V lithium-ion battery chemistry. *Energy &*
605           *Environmental Science* **6**, 1806-1810 (2013).

606

607    32.    Markevich E, *et al.* Fluoroethylene Carbonate as an Important Component in Electrolyte
608           Solutions for High-Voltage Lithium Batteries: Role of Surface Chemistry on the Cathode.
609           *Langmuir* **30**, 7414-7424 (2014).

610

611    33.    Smart MC, Ratnakumar BV, Surampudi S. Use of Organic Esters as Cosolvents in
612           Electrolytes for Lithium-Ion Batteries with Improved Low Temperature Performance.
613           *Journal of The Electrochemical Society* **149**, A361 (2002).

614

615    34.    Chen X, Li L, Liu M, Huang T, Yu A. Detection of lithium plating in lithium-ion batteries by
616           distribution of relaxation times. *Journal of Power Sources* **496**, 229867 (2021).

617

618    35.    Schmidt JP, Berg P, Schönleber M, Weber A, Ivers-Tiffée E. The distribution of relaxation
619           times as basis for generalized time-domain models for Li-ion batteries. *Journal of Power*
620           *Sources* **221**, 70-77 (2013).

621

622    36.    Zhou X, Huang J, Pan Z, Ouyang M. Impedance characterization of lithium-ion batteries
623           aging under high-temperature cycling: Importance of electrolyte-phase diffusion. *Journal*
624           *of Power Sources* **426**, 216-222 (2019).

625

626    37.    Lu Y, Zhao C-Z, Huang J-Q, Zhang Q. The timescale identification decoupling
627           complicated kinetic processes in lithium batteries. *Joule* **6**, 1172-1198 (2022).

628

629    38.    Lu Y, *et al.* The carrier transition from Li atoms to Li vacancies in solid-state lithium alloy

anodes. *Science Advances* **7**, eabi5520 (2021).

39. Mo Y, *et al.* Engineering Electrode/Electrolyte Interphase Chemistry toward High-Rate and Long-Life Potassium Ion Full-Cell. *ACS Energy Letters*, 995-1002 (2023).

40. Illig J, Ender M, Weber A, Ivers-Tiffée E. Modeling graphite anodes with serial and transmission line models. *Journal of Power Sources* **282**, 335-347 (2015).

41. Yao Y-X, *et al.* Regulating Interfacial Chemistry in Lithium-Ion Batteries by a Weakly Solvating Electrolyte**. *Angewandte Chemie International Edition* **60**, 4090-4097 (2021).

42. Cao C, *et al.* Toward Unraveling the Origin of Lithium Fluoride in the Solid Electrolyte Interphase. *Chemistry of Materials* **33**, 7315-7336 (2021).

43. Lan X, Cui J, Xiong X, He J, Yu H, Hu R. Multiscale Observations of Inhomogeneous Bilayer SEI Film on a Conversion-Alloying SnO2 Anode. *Small Methods* **5**, 2101111 (2021).

44. Schroder KW, Dylla AG, Harris SJ, Webb LJ, Stevenson KJ. Role of Surface Oxides in the Formation of Solid–Electrolyte Interphases at Silicon Electrodes for Lithium-Ion Batteries. *ACS Applied Materials & Interfaces* **6**, 21510-21524 (2014).

45. Tan J, Matz J, Dong P, Shen J, Ye M. A Growing Appreciation for the Role of LiF in the Solid Electrolyte Interphase. *Advanced Energy Materials* **11**, 2100046 (2021).

46. Xue W, *et al.* Ultra-high-voltage Ni-rich layered cathodes in practical Li metal batteries enabled by a sulfonamide-based electrolyte. *Nature Energy* **6**, 495-505 (2021).

47. Petzl M, Danzer MA. Nondestructive detection, characterization, and quantification of lithium plating in commercial lithium-ion batteries. *Journal of Power Sources* **254**, 80-87 (2014).

48. P. J. Stephens. F. J. Devli. C. F. Chabalowski MJF. Ab Initio Calculation of Vibrational Absorption and Circular Dichroism Spectra Using Density Functional Force Fields. *J Phys Chem C* **98**, 5 (1994).

49. Krishnan R, Binkley JS, Seeger R, Pople JA. Self-consistent molecular orbital methods. XX. A basis set for correlated wave functions. *The Journal of Chemical Physics* **72**, 650-654 (1980).

50. Sun H, *et al.* COMPASS II: extended coverage for polymer and drug-like molecule databases. *Journal of Molecular Modeling* **22**, 47 (2016).

51. Shuichi N. Constant Temperature Molecular Dynamics Methods. *Progress of Theoretical Physics Supplement* **103**, 1-46 (1991).

# Supplementary Files

This is a list of supplementary files associated with this preprint. Click to download.

- MovieS1ElectricfanpoweredwithEHFBelectrolyteat100XXX.mov
- MovieS2FailedtobepoweredwithBaseelectrolyteat86XXX.mov
- SupportingInformation.docx